strain
An International Journal for Experimental Mechanics

A Point-wise Approach to the Analysis of Complex Composite Structures Using Digital Image Correlation and Thermoelastic Stress Analysis

G. Crammond, S. W. Boyd and J. M. Dulieu-Barton

Faculty of Engineering and the Environment, University of Southampton, University Road, Southampton, SO17 1BJ, UK

ABSTRACT: Thermoelastic stress analysis (TSA) and digital image correlation (DIC) are used to examine the stress and strain distributions around the geometric discontinuity in a composite double butt strap joint. A well-known major limitation in conducting analysis using TSA is that it provides a metric that is only related to the sum of the principal stresses and cannot provide the component stresses/strains. The stress metric is related to the thermoelastic response by a combination of material properties known as the thermoelastic constant (coefficient of thermal expansion divided by density and specific heat). The thermoelastic constant is usually obtained by a calibration process. For calibration purposes when using orthotropic materials, it is necessary to obtain the thermoelastic constant in the principal material directions, as the principal stress directions for a general structure are unknown. Often, it is assumed that the principal stress directions are coincident with the principal material directions. Clearly, this assumption is not valid in complex stress systems, and therefore, a means of obtaining the thermoelastic constants in the principal stress directions is required. Such a region is that in the neighbourhood of the discontinuities in a bonded lap joint. A methodology is presented that employs a point-wise manipulation of the thermoelastic constants from the material directions to the principal stress directions using full-field DIC strain data obtained from the neighbourhood of the discontinuity. A comparison of stress metrics generated from the TSA and DIC data is conducted to provide an independent experimental validation of the two-dimensional DIC analysis. The accuracy of a two-dimensional plane strain finite element model representing the joint is assessed against the two experimental data sets. Excellent agreement is found between the experimental and numerical results in the adhesive layer; the adhesive is the only component of the joint where the material properties were not obtained experimentally. The reason for the discrepancy is discussed in the paper.

KEY WORDS: *adhesive bonding, composite, digital image correlation, materials, thermoelastic stress analysis*

Introduction

Adhesive bonding provides an efficient, low weight, solution for the joining of composite components [1]. Joints present a significant engineering design challenge as they contain discontinuities in geometry and material properties. Composite joints are strong in the in-plane fibre direction but are weak normal to the plane of the laminate, as the strength is dominated by the mechanical properties of the polymer matrix [2]. Hence, the weak through-thickness properties, and the relatively high through-thickness stresses across the discontinuity, make the laminate susceptible to the initiation of interlaminar cracks, which lead to failure of the adhesively bonded joint [1].

Full-field experimental techniques such as thermoelastic stress analysis (TSA) [3] and digital image correlation (DIC) [4] have been used to analyse the stress and strain distributions in complex composite structures such as adhesively bonded joints, for example, [5–10]. TSA and DIC data have been used for material characterisation during dynamic loading [11], for analysis of complex structures with heterogeneous material properties [12] and for the monitoring of damage growth in composites [13]. DIC has also been undertaken in combination with infrared thermography in the development of thermomechanical models of metals [14–17]. Although TSA and DIC have both been used to assess mechanical behaviour of materials and structures, the idea of combining the techniques is relatively new. DIC has been integrated into the methodologies of TSA [18] to correct for rigid body motions. Displacement data have also been successfully obtained from correlating sequences of infrared images [19, 20] and then applying DIC, hence removing the need for separate cameras to use DIC for motion compensation.

In the present paper, TSA and DIC are combined to provide a data-rich analysis of a double butt strap joint (DBSJ). The independent experimental data sets are used to verify the results from each technique and to validate a two-dimensional (2D) finite element model of the joint.

Specimen Definition

Geometry

The DBSJ was constructed with low crimp Gurit UT-E 800 g m^{-2} (Gurit, Newport, UK) unidirectional (UD) glass fibre and 450 g m^{-2} M79 chopped strand mat (CSM) (PPG Fibre Glass, Zibo, China) glass fibre in a $[CSM_8\ 90_4]_s$ sequence using Gurit Prime 20LV epoxy resin and the resin infusion process. The materials and stacking sequence create thick layers of dissimilar material, providing sufficient thickness across each material layer for a large number of data points

doi: 10.1111/str.12142

to be captured with the infrared and white light detectors used in this investigation. Figure 1 shows the DBSJ, which was 25 mm in the *z*-direction. The inner adherends of the DBSJ were 150 mm long, separated by a 2-mm gap at the butt between the adherends. The outer adherends were 75 mm long, producing an asymmetric joint with overlap lengths of 25 and 50 mm. The DBSJ geometry ensures that failure initiation occurs at the discontinuity with the smaller overlap, which can be observed over small length scales imaged as indicated in Figure 1 by both the TSA and DIC. Araldite 2015 (Basel, Switzerland), a toughened structural epoxy adhesive, was used to bond the adherends. Adhesive spew fillets were removed during manufacture to facilitate a large stress concentration at the discontinuity. The large stress concentration is required to generate a relatively large strain in the through-thickness direction, which can be accurately measured using DIC.

In Figure 1, the principal material directions of the DBSJ constituents are not indicated as these are different for the CSM and UD layers. The plane of observation of the joint during the tests is the *x*–*y* plane indicated in Figure 1. The plane of observation is the 2, 3 material directions for the UD and the 1, 3 material direction for the CSM; that is, the UD material is quasi-isotropic and the CSM is orthotropic in the *x*–*y* plane. The nomenclature 1^p and 2^p indicate the principal stress directions in the observation plane—the angle of these axes to the material axes, θ^p, varies depending on the location in the joint. It is important to note that, away from the discontinuity, the principal material directions in the CSM and the principal stress directions are coincident.

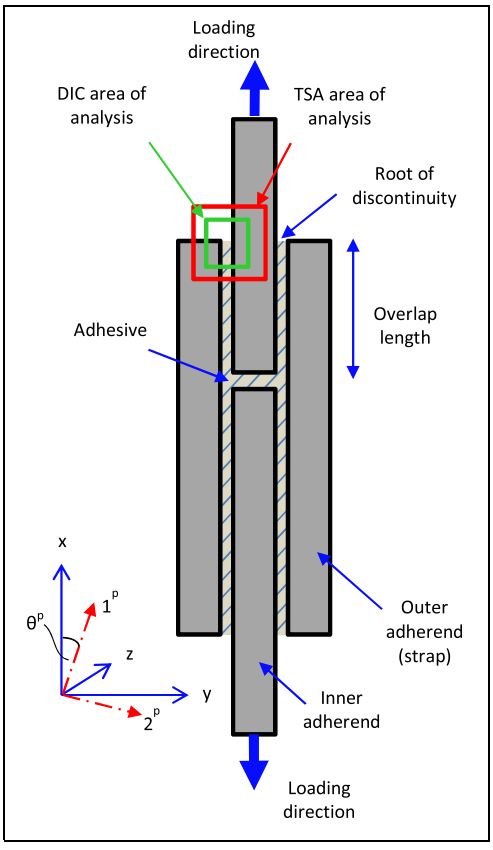

Figure 1: Schematic of double butt strap joint.

Material properties

Figure 2 shows an overview of the specimens, fibre directions and loading configurations used to obtain the material properties for the DBSJ construction. Specimens were made only for the CSM constituent for the configuration shown in Figure 2A, C and D. Specimens were constructed for both CSM constituent and the UD constituent in the configurations shown in Figure 2B. These five specimens provided all the material properties necessary to conduct the analysis described in later sections of the paper. For each configuration and material type, the material directions are indicated in Figure 2. For the UD material, the 1 direction is parallel to the fibres, the 2 direction is transverse to the fibres and the 3 direction is transverse to the layers. For the CSM material, the 1 and 2 directions are in the plane of the random orientation where the 1 direction is parallel to the layers, and the 3 direction is transverse to the layers. It is important to note that 1, 2 and 3 for the CSM material are not conventional 'principal material directions' as used in orthotropic fibre reinforced polymer lamina elasticity analysis but a notation adopted for convenience.

The specimens shown in Figure 2A are ASTM D3039 coupons, which were used to provide E_1 for the CSM. The specimens were manufactured from six layers of 450 g m^{-2} CSM material consolidated using Gurit Prime 20LV epoxy resin and the resin infusion method. The specimens were loaded at a displacement rate of 2 mm min^{-1} in an Instron 5569 electro-mechanical test machine (Instron, Norwood, MA, USA). The strains in the specimen longitudinal direction were obtained using an Instron 2630-113 clip gauge extensometer (Instron) with a 50-mm gauge length.

The E_3 of the CSM material and E_3 for the UD were evaluated from DIC analysis of a high-aspect-ratio parallel-sided coupon as shown in Figure 2B. The specimens were manufactured from a number of thick $[CSM]_{16}$ and $[90]_{20}$ specimens bonded together using Araldite 2015 into a stack between two aluminium end blocks. A set of universal joints were used to connect the specimen to the test machine to minimise specimen bending. The loading sequence was imaged using a 5-Mp LaVision E-Lite camera (Goettingen, Germany) and a Sigma 105-mm lens (Sigma-Aldrich Corporation, St. Louis, MO, USA) delivering a spatial resolution of 59.5 pixels mm^{-1}. The DIC analysis was

© 2015 Wiley Publishing Ltd | *Strain* (2015) **51**, 311–323
doi: 10.1111/str.12142

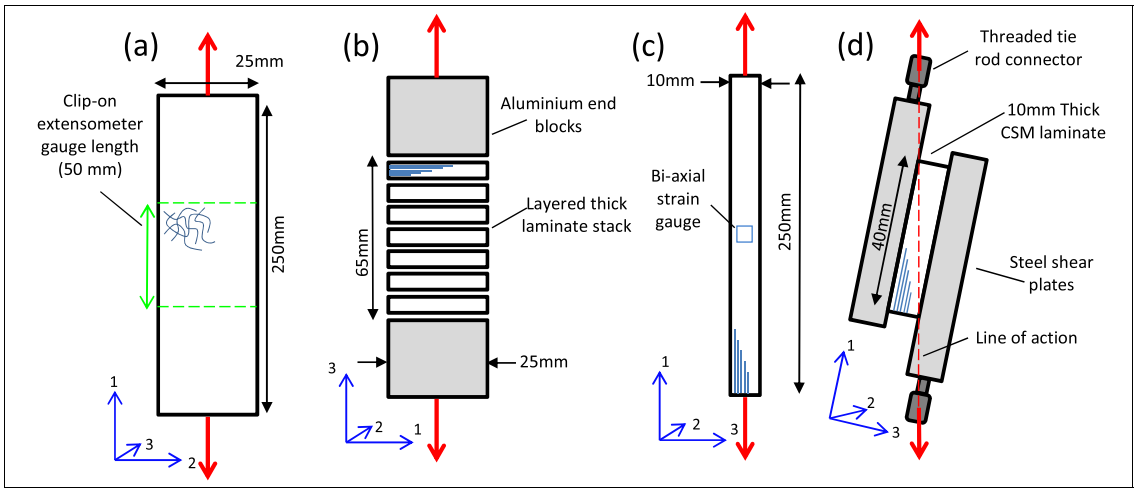

Figure 2: Schematic of the material property test coupons

conducted using DAVIS 7.4 (Goettingen, Germany), which employs a cross-correlation algorithm using inverse fast Fourier transforms, with a subset size of 64 × 64 pixels. Subpixel displacement accuracy is obtained through the fitting of a 2D Gaussian parameter to the correlation function peak. Strains are evaluated from the deformation vectors using a central difference approach.

Poisson's ratio, v_{13}, for the CSM material was obtained from Tokyo Sokki Kenkyujo Co FCA-3-32 biaxial strain gauges (Tokyo Sokki Kenkyujo Co., Ltd, Tokyo, Japan) bonded onto the side of an 8-mm-thick ASTM D3039 coupons, shown in Figure 2C. The gauges had a gauge length of 3 mm, and the specimens were manufactured from 16 layers of CSM material. A manipulation of the E_1, E_3, obtained from the specimens shown in Figure 2A and B, and v_{13} values were used to evaluate the v_{31} Poisson ratio.

The G_{13} shear modulus for the CSM was obtained from analysis of 8-mm-thick CSM laminate coupons measuring 40 × 40 mm bonded between two steel shear plates using Araldite 2015 (Figure 2D). The specimens were fixed to an Instron 5569 test machine (Instron) using a threaded tie rod with a universal end joint, such that the line of action of the load passes through opposite corners of the specimen, loading the specimen in pure shear. The specimen shear strains were recorded from 2D DIC analysis with a spatial resolution of 38 pixels mm^{-1} with subset size of 79 × 79 pixels in DAVIS 8.0.

A summary of the material properties and standard deviations is given in Table 1, with reference to the observation plane (x–y) and to the material axes. It can be seen that the UD material in the observation plane is practically isotropic. The Poisson ratio for the UD material was obtained from the literature [21] and the G value calculated assuming an isotropic material. Material properties for the Araldite adhesive were taken from private communications with Huntsman [22, 23] regarding the isotropic nature of the material and the values quoted in their datasheet [24].

Initial Digital Image Correlation Results

Two-dimensional DIC was conducted to obtain the strains generated over the area shown in Figure 1. This region was chosen for analysis as the geometric discontinuity generates large load path eccentricity between the adherends, which leads to the initiation of damage through the formation of high-through-thickness strains. A 5-Mp LaVision E-Lite camera fitted with a high-magnification Canon MP-e65 macro lens (Canon Inc., Tokyo, Japan) mounted on an X–Y–θ adjustable mount was used to image the area shown in Figure 1, measuring 3.1 × 2.6 mm. The macro lens allows a high spatial resolution image to be obtained, allowing large, high strain precision [25] subsets to be used in the DIC processing without compromising on the spatial resolution of the data. This methodology is very similar to that used in [26]. The limitations of using the macro lens are that only a small region of interest can be viewed with a short focal distance. As a result, only a single-camera, 2D DIC set-up can be used, and therefore, the effect of out-of-plane displacements could not be removed from the in-plane

Table 1: Material property values for CSM and 90° material

Image plane values (x–y)	CSM	UD	Araldite 2015
E_x (GPa)	$E_1 = 11.27 \pm 0.72$	$E_2 = 20.14 \pm 1.49$	2.09 [22]
E_y (GPa)	$E_3 = 7.63 \pm 0.57$	$E_3 = 20.14 \pm 1.49$	2.09 [22]
v_{xy}	$v_{13} = 0.34 \pm 0.01$	0.34 [21]	0.36 [24]
v_{yx}	$v_{31} = 0.23$	0.34 [21]	0.36 [24]
G_{xy} (GPa)	$G_{13} = 2.42 \pm 0.43$	7.51	0.74 [23]

doi: 10.1111/str.12142

strain measurement. The stochastic speckle pattern was applied using black paint from a fine nozzle airbrush onto a white background in order to minimise measurement error [27]. Images with a resolution of 684 pixels mm^{-1} were captured at a 5-Hz framing rate as the joint was loaded at 2 mm min^{-1} in an Instron 5569 test machine. Image correlation and displacement/strain evaluation were conducted using the DaVis 7.4 software. The same correlation algorithms as noted in the Material Properties section were used. A subset size of 128 × 128 pixels with a 50% subset overlap provides a spatial resolution of approximately three data points per millimetre.

The localised strain distributions around the discontinuity obtained by correlating between images at 0 and 6 kN are shown in Figure 3A–C. The results show similar trends to experimental results in literature [28, 29], providing confidence in the accuracy of the experimental set-up. The largest axial strains are identified in the inner adherend, decreasing across the span of the joint as load is transferred across adhesive layer into the outer straps. At this relatively low load level, the through-thickness deformations are small, making strain measurement with DIC difficult. Nevertheless, two peel strain concentrations in the inner and outer adherends either side of the adhesive layer can be identified. The peel strain concentration in the inner adherend is smaller compared with the outer strap, due to the local constraint on the material deformation imposed by the surrounding material in the inner adherend. Figure 3C clearly shows that the load transfer between adherends is achieved by shear of the adhesive layer. A decrease in shear strain close to the root of the discontinuity is visible, which is associated with the zero shear stress conditions at the end of the adherend. Figure 3 also identifies axial and peel strains manifested along the adhesive interfaces due to the transition of load across the shear-loaded adhesive.

The DIC results form a basis understanding of the load transfer in the joint around the discontinuity. Highly localised features and complex structural responses can be observed, which determines the structural performance of the joint. The features around the geometric discontinuity are highly localised and even at the high magnifications used may be smoothed by the DIC, hence the requirement to obtain stress distributions in the DBSJ using TSA.

Thermoelastic Stress Analysis

Methodology

Thermoelastic stress analysis is an experimental technique based on the relationship between the material deformation and the thermal energy of a solid under loading known as the thermoelastic effect. At the same instance as a material or component experiences a stress change, a small temperature change also occurs. Loading is applied cyclically in the linear elastic region at such a rate that isentropic conditions prevail. A highly sensitive infrared detector is used to measure the change in temperature experienced, ΔT, on the specimen surface due to the thermoelastic effect in addition to the mean specimen temperature during testing, T. The relationship between the temperature measurements ΔT and T and the product of the stress and coefficient of thermal expansion tensors in the principal stress, principal material and in the joint axes (x–y, i.e. the image plane as shown in Figure 1) is as follows for an orthotropic material [3, 30]:

$$\Delta T = -\frac{T}{\rho C_p}\,[\alpha^p]_{1,2}[\sigma^p]_{1,2} = -\frac{T}{\rho C_p}\,[\alpha]_{1,2}[\sigma]_{1,2} = -\frac{T}{\rho C_p}\,[\alpha]_{x,y}[\sigma]_{x,y} \quad (1)$$

where ρ is the material density and C_p is the specific heat capacity at constant pressure and

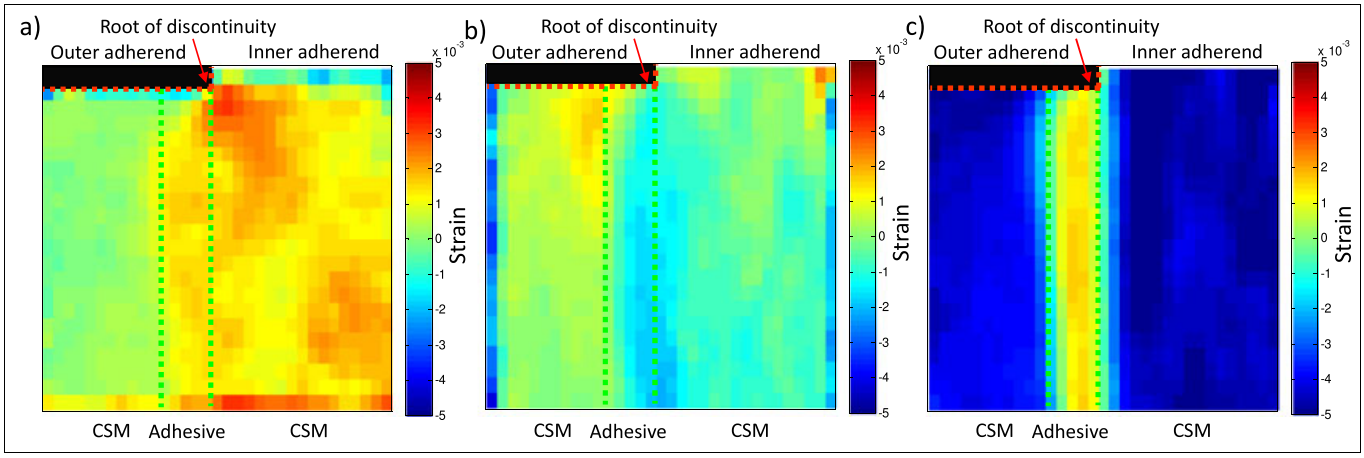

Figure 3: (a) Axial, (b) peel and (c) shear strain around the geometric discontinuity at 6-kN load

© 2015 Wiley Publishing Ltd | *Strain* (2015) **51**, 311–323
doi: 10.1111/str.12142

$$[\alpha^p]_{1,2} = \begin{bmatrix} \alpha_1^p \\ \alpha_2^p \\ \alpha_6^p \end{bmatrix}, \quad [\alpha]_{1,2} = \begin{bmatrix} \alpha_1 \\ \alpha_2 \\ \alpha_6 \end{bmatrix}, \quad [\alpha]_{x,y} = \begin{bmatrix} \alpha_x \\ \alpha_y \\ \alpha_{xy} \end{bmatrix} \tag{2}$$

$$[\sigma^p]_{1,2} = \begin{bmatrix} \sigma_1^p \\ \sigma_2^p \\ \sigma_6^p \end{bmatrix}, \quad [\sigma]_{1,2} = \begin{bmatrix} \sigma_1 \\ \sigma_2 \\ \tau_6 \end{bmatrix}, \quad [\sigma]_{x,y} = \begin{bmatrix} \sigma_x \\ \sigma_y \\ \sigma_{xy} \end{bmatrix} \tag{3}$$

The relationship between these values and the coefficient of thermal expansions is often expressed as 'thermoelastic constants', K, as given by the following equation:

$$[K^p]_{1,2} = \frac{1}{\rho C_p}[\alpha^p]_{1,2}, \quad [K]_{1,2} = \frac{1}{\rho C_p}[\alpha]_{1,2}, \quad [K]_{x,y} = \frac{1}{\rho C_p}[\alpha]_{x,y} \tag{4}$$

Equations (1) and (4) combine to give the following relationship between the temperature change and the changes in the principal, material and joint axis stresses:

$$\frac{\Delta T}{T} = -[K^p]_{1,2}[\sigma^p]_{1,2} = -[K]_{1,2}[\sigma]_{1,2} = -[K]_{x,y}[\sigma]_{x,y} \tag{5}$$

Equation (5) means that the thermoelastic response is not a function of the material directions as ΔT and T are scalar quantities. Therefore, the product of the thermoelastic and stress terms in any axis system must be equal as follows:

$$\begin{aligned} \frac{\Delta T}{T} &= -\left(K_1^p \Delta\sigma_1^p + K_2^p \Delta\sigma_2^p\right) = -(K_1\Delta\sigma_1 + K_2\Delta\sigma_2) \\ &= -\left(K_x\Delta\sigma_x + K_y\Delta\sigma_y + K_{xy}\Delta\sigma_{xy}\right) \end{aligned} \tag{6}$$

Mathematically, the determination of Equation (6) from Equation (5) is only correct when the shear terms are retained. However, there are two situations in a stress system when the shear terms can be neglected. The first is when working in the principal stress plane, where the shear stress is zero, that is, $\sigma_6^p = 0$. The second is in the principal material plane where the shear coefficient of thermal expansion is zero, that is, $\alpha_6 = 0$, and hence, the 'thermoelastic shear constant' is also zero, that is, $K_6 = 0$.

A more useful form of Equation (6) is to manipulate it into the commonly used form of a 'stress metric (SM)'; for the principal stresses, the SM is as follows [3]:

$$\mathrm{SM}_1 = \frac{\Delta T}{K_1^p T} = \Delta\sigma_1^p + \frac{K_2^p}{K_1^p}\Delta\sigma_2^p \tag{7}$$

K_1^p appears on the left-hand side of Equation (7), making the SM a tensor quantity. A similar rearrangement allows an SM to be expressed in terms of the stresses in the principal material directions or the joint axes:

$$\mathrm{SM}_2 = \frac{\Delta T}{K_1 T} = \Delta\sigma_1 + \frac{K_2}{K_1}\Delta\sigma_2 \tag{8}$$

$$\mathrm{SM}_3 = \frac{\Delta T}{K_x T} = \Delta\sigma_x + \frac{K_y}{K_x}\Delta\sigma_y + \frac{K_{xy}}{K_x}\Delta\sigma_{xy} \tag{9}$$

It is possible to use SM_1, SM_2 or SM_3 as an SM for comparison with model data. In previous work [5–7] which has applied TSA to analyse components manufactured from othotropic materials, the K values have been derived in the principal material directions, and SM_2 has been used. In some cases, it can be assumed that the principal stress and principal material directions are coincident [31] and that the reference axes are coincident to the material directions, whereby $\mathrm{SM}_1 = \mathrm{SM}_2 = \mathrm{SM}_3$. It is clear from Equations [7–9] that, in situations where these coordinate systems are not coincident, the SMs are different, that is, $\mathrm{SM}_1 \neq \mathrm{SM}_2 \neq \mathrm{SM}_3$.

In the present case, the image plane is the x–y plane, which is not necessarily the principal material plane because of the laminate construction (see above); hence, it should be considered that K_{xy} may be finite. An example of a similar situation is given in [32] when a pure shear load was applied to a composite cylinder and finite thermoelastic response was detected. Therefore, in the present paper, the premise that $K_{xy} \neq 0$ is explored; therefore, the formulation of the SM given in Equation (9) must be used. However, the value of K_{xy} has not been evaluated; hence, it is convenient to transform the analysis from the joint x–y axis to the principal stress axes to enable the use of SM_1 in the analysis and eliminate the shear term.

To obtain SM_1, it is necessary to derive the thermoelastic constants in the principal stress directions. For a complex orthotropic component, this is not a straightforward matter as the principal stress directions will change point by point. Hence, in the following section, a methodology is proposed that enables a point-by-point determination of the principal stress directions using DIC and hence the determination of the thermoelastic constant in these directions. In the present work, Equation (7) only applies to the CSM layer and not to the UD or adhesive layers as these are isotropic in the plane of observation. Here, there is only one K value and $\left(\sigma_1^p + \sigma_2^p\right) = \left(\sigma_x + \sigma_y\right)$, so there is no need to establish the direction of the principal stresses in these parts of the joint.

Derivation of thermoelastic constants

The starting point to the determination of the thermoelastic constants in the principal stress directions, required for Equation (7), is to obtain the thermoelastic constants in the principal material directions. The K_x and K_y thermoelastic

doi: 10.1111/str.12142

constants in the principal material direction are obtained by loading the specimens uniaxially in either the x or y direction, such that only one stress term remains in Equation (9) to give

$$K_x = \frac{\Delta T}{T\Delta\sigma_x} \tag{10}$$

$$K_y = \frac{\Delta T}{T\Delta\sigma_y} \tag{11}$$

The thermoelastic constants given in Equations (10) and (11) can be obtained through materials coupon tests using the applied load level and recorded temperature data. In this case, it is essential that the principal material directions are coincident with the principal stress directions, which can be achieved by using the material coupon test specimens in Figure 2B and C.

K_x for the CSM material was evaluated experimentally from four 10-mm-thick tensile coupons measuring 200×25 mm cut from a $[CSM]_{16}$ laminate, as shown in Figure 2C. The specimens were loaded with a mean load of 8 kN with an amplitude of 4 kN at 20 Hz in an Instron 8800 servo-hydraulic test machine. Measurements were recorded from two 4×25 mm areas in the 1–3 material plane to obtain average values of ΔT and T. K_y was evaluated using a similar approach to that presented in [7]. Four $25 \times 25 \times 70$ mm, high-aspect-ratio specimens constructed from a stack of 10-mm-thick $[CSM]_{16}$ laminate sections, as shown in Figure 2B, were loaded with a mean load of 3 kN with an amplitude of 2.5 kN at 20 Hz in an Instron 8800 servo-hydraulic test machine. The high-aspect-ratio specimens provide a more uniform stress field across the measurement surface compared with those used in [7], providing more representative K_y calculation. The response of the adhesive layers between the stacked laminates was neglected in the analysis.

The K value for the UD glass fibre material was established from high-aspect through-thickness specimens constructed from a stack of thick $[90]_{20}$ laminate coupons, using the same test procedures described in the Material Properties section for the specimen in Figure 2B. It was not necessary to apply a high emissivity paint coating as the emissivity of the glass fibre composite was sufficient to enable measurement. A summary of the derived thermoelastic constants is provided in Table 1.

Thermoelastic stress analysis

The TSA was conducted using a high-resolution G1 macro lens fitted to a Flir Silver SC5000 320×256 indium antimonide infrared detector array (Wilsonville, Oregon, USA). An area approximately 7×5.7 mm, as shown in Figure 1 around the discontinuity between the inner and outer straps, was imaged. This is a similar mesoscopic length scale as the DIC and produces a spatial resolution of 45 pixels mm^{-1}. The joint was loaded at 20 Hz with a mean load of 6 kN and a loading amplitude of 3 kN in an Instron 8800 servo-hydraulic test machine, generating a load range of 6 kN, equivalent to the load step used to obtain the DIC data in Figure 3. The infrared detector was connected to the load output of the test machine to enable a lock-in process to be used to obtain ΔT and provide mean surface temperature data, that is, T. Due to the small field of view, the cyclic loading produces a relatively large motion of the specimen over the image area. Therefore, the Flir random motion compensation function within the Flir Altair software (Wilsonville, Oregon, USA) was used to compensate for the movement of the specimen during testing and ensure accurate measurements.

A plot of the $\Delta T/T$ values around the discontinuity can be seen in Figure 4A. The texture observed in the plot identifies the variable orientation of the CSM fibres aligned out of the page and rough surface finish from preparing the specimen. An area of high thermoelastic response is seen at the root of the discontinuity within the CSM layer of the inner adherend and within the adhesive layer where the geometric discontinuity is most severe.

Multiplying the temperature data in Figure 4A by the $1/K_1$ values given in Table 2 as appropriate for the CSM or UD/Adhesive layers, respectively, delivers the full-field plot of the SM_2 derived in Equation (8) (Figure 4B). Applying the thermoelastic constants significantly changes the appearance of the full-field data. As the adhesive layer is loaded mainly in shear, the SM_2 in the adhesive is very small.

To obtain SM_1 given in Equation (7) for the CSM layers, it is necessary to derive the principal stresses. This was achieved by obtaining the material stresses in the joint from manipulation of the experimental 2D mesoscale DIC strain data in Figure 3. The principal stress directions were then evaluated from these material stresses from a Mohr's circle analysis, which was used to transform the material stresses to the principal axes using the following relationships:

$$\begin{bmatrix} \sigma_x \\ \sigma_y \\ \tau_{xy} \end{bmatrix} = [Q]_{xy} \begin{bmatrix} \varepsilon_x \\ \varepsilon_y \\ \gamma_{xy} \end{bmatrix} \tag{12}$$

$$\tan 2\theta^p = \frac{2\tau_{xy}}{\sigma_x - \sigma_y} \tag{13}$$

$$\begin{bmatrix} \sigma_1^p \\ \sigma_1^p \\ 0 \end{bmatrix} = [T]^{-1} \begin{bmatrix} \sigma_x \\ \sigma_y \\ \tau_{xy} \end{bmatrix} \tag{14}$$

where $[Q]_{xy}$ is the stiffness matrix in the plane of observation for the materials in the CSM layer determined

doi: 10.1111/str.12142

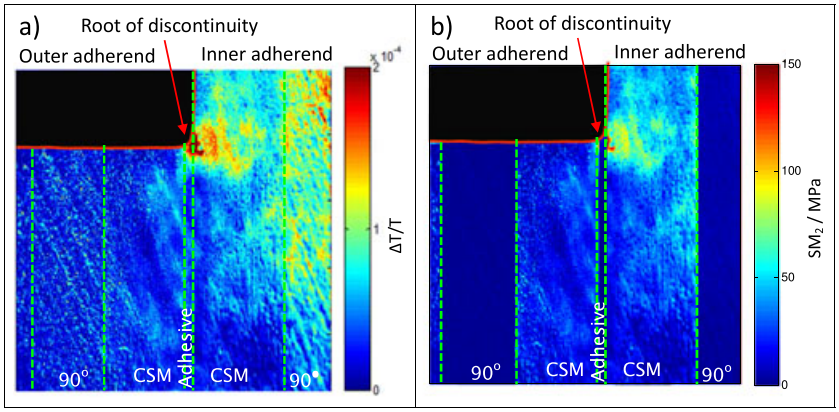

Figure 4: (a) Raw $\Delta T/T$ infrared data and (b) process thermoelastic stress analysis SM

Table 2: Thermoelastic constants

Material	K_x thermoelastic constant (MPa^{-1})	K_y thermoelastic constant (MPa^{-1})
CSM	$2.10 \times 10^{-6} \pm 7.44 \times 10^{-7}$	$4.47 \times 10^{-5} \pm 4.01 \times 10^{-6}$
UD	$2.17 \times 10^{-5} \pm 1.37 \times 10^{-6}$	$2.17 \times 10^{-5} \pm -1.37 \times 10^{-6}$
Araldite 2015	2.88×10^{-5} [6]	2.88×10^{-5} [6]

from the values in Table 1 and $[T]$ is the transformation matrix using the principal stress direction θ^p [2, 32]. A similar approach to determine the principal stresses from DIC component strains is used in [26]. The principal stress directions obtained from the DIC strain data are shown in Figure 5.

Once the principal stress direction, θ^p, is known for any given data point using the Mohr's circle analysis of the material stresses, it is possible to transform the thermoelastic constants using the following expression:

$$\begin{bmatrix} K_1^p \\ K_2^p \\ K_6^p \end{bmatrix} = [T]^T \begin{bmatrix} K_x \\ K_y \\ K_{xy} \end{bmatrix} \tag{15}$$

As the principal stress direction varies across the field of view around the discontinuity, the transformations are conducted on a point-wise basis for each data point. SM_1 given in Equation (7) is then established for the CSM material by multiplying the $\Delta T/T$ values by $1/K_1^p$ for each data point.

The variation in the thermoelastic constant with the principal stress direction is shown in Figure 6A. Here, $1/K_1^p$ is plotted against θ^p, where it can be seen that small departures from the principal material direction result in large changes to the thermoelastic constant. In Figure 6B, the effect on the quantity K_2^p/K_1^p is shown. A departure of as little as 10° from the principal material directions results in a 50% decrease in both $1/K_1^p$ and K_2^p/K_1^p. This therefore demonstrates that the derivation of the correct thermoelastic constants is essential to generate the SM in Equation (7). The rate and shape of the changes in thermoelastic ratio are clearly dependent on the orthotropy of the material.

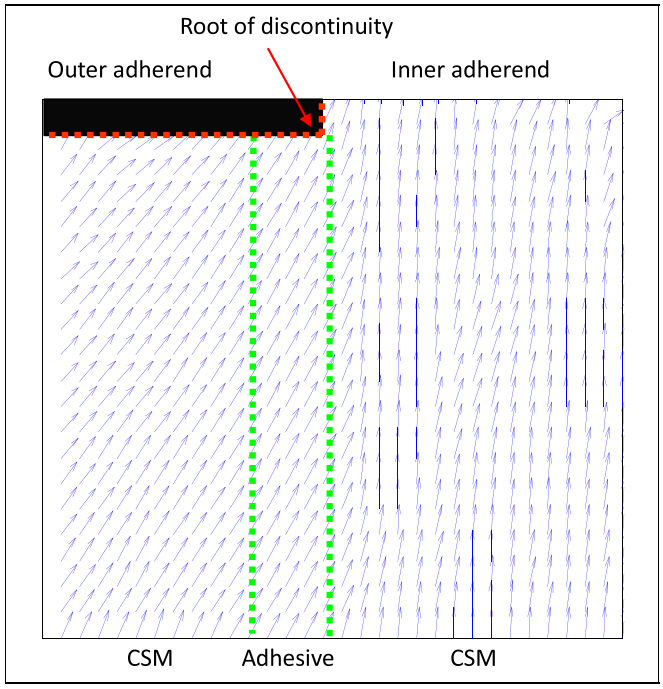

Figure 5: Principal stress directions around the discontinuity

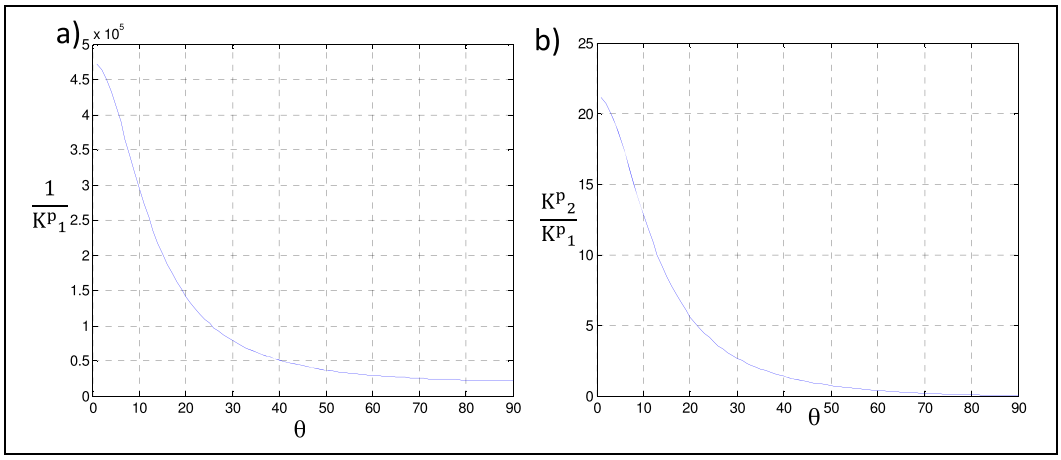

Figure 6: Response of (a) $1/K^p_1$ and (b) K^p_2/K^p_1 thermoelastic constants transformed away from the material axis

Comparison of Experimental Digital Image Correlation and Thermoelastic Stress Analysis Stress Metrics

The area of interest and spatial resolution of the TSA data are greater than those of the DIC. Therefore, it is necessary to crop the region of interest and downsample the TSA data by an integer factor of 3 to give approximately the same spatial resolution and area of interest as the DIC data. This ensures that the transformed thermoelastic constants are applied to the correct location in the joint. SM_1 for the DIC data was established by applying the material properties in Table 1 to the strain data, providing the coordinate stresses (see Equation (12)) and then using Equations (13) and (14) to determine the principal stresses. The second principal stress was then multiplied by K^p_2/K^p_1, to generate SM_1 given by Equation (7). The thermoelastic values used were obtained from the transformation of the material thermoelastic constants in Table 2 into the principal stress directions using Equation (15) and θ^p, which was determined from Mohr's circle analysis of the material stresses evaluated from the DIC data, Equations [12–14]. As the principal stress direction is different across the joint, this calculation was repeated for each data point in the image.

The SM_1 values generated for the TSA and DIC data are shown in Figure 7A and B, respectively. Although the two techniques use independent data sources, it should be noted that the manipulation of both techniques is dependent on obtaining the principal stress directions from the DIC. Therefore, inaccuracies in the calculation of the stresses and θ^p from the DIC strains are also introduced into SM_1 for the TSA data through the transformation of the thermoelastic constants. Hence, the SM_1 values, derived from the DIC and the TSA, are no longer truly independent quantities. A confirmation that the principal stress directions derived from the DIC are correct could be obtained from further experimental analysis such as Moiré interferometry or electronic speckle pattern interferometry. This was not done in the present work as the good agreement between the two data sets and the finite element analysis described later in the paper provide sufficient validation without recourse to further experimentation. Figure 7A and B shows very good qualitative agreement, capturing the location and magnitude of SM_1 around the complex geometry in the neighbourhood of the discontinuity. The largest SM_1 values are located within an area approximately 0.5×0.5 mm of the inner adherend at the root of the discontinuity, similar to that seen in Figure 4B. The size of the stress concentration in the inner adherend is very similar between both techniques, reducing quickly away from the discontinuity towards the centre of the joint, identifying the powerful stress-concentrating influence of the geometric discontinuity.

The agreement between the two data sets is best shown in Figure 8A and B, where a line plots through the two data sets along lines A and B in Figure 7, 0.03 and 0.093 mm from the end of the outer adherend. Low SM_1 values are observed along lines A and B in the outer adherend. An increase in the DIC SM_1 is seen at the adhesive interface with the outer adherend, which is not apparent in the TSA SM_1 data, because the lower-resolution DIC does not capture the high peel and interfacial axial and shear strains as shown in Figure 3. The SM_1 values for both techniques are low across the shear-loaded adhesive layer before experiencing a sharp increase in stress around the discontinuity in the inner adherend. This stress peak is a function of both the stress-concentrating effect around the sharp discontinuity and the increased axial loading in the inner adherend. The stress peak in the inner adherend is captured very well in both plots, with both techniques observing similar

doi: 10.1111/str.12142

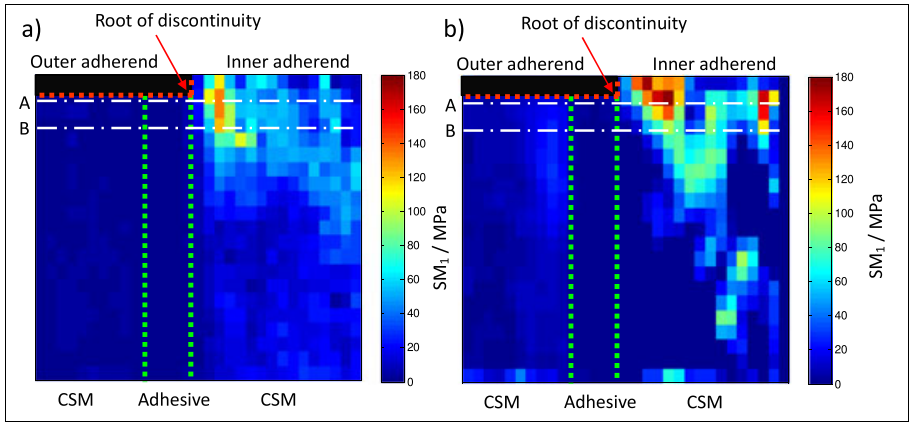

Figure 7: Directly comparable (a) thermoelastic stress analysis and (b) digital image correlation stress metrics (SMs) around the geometric discontinuity

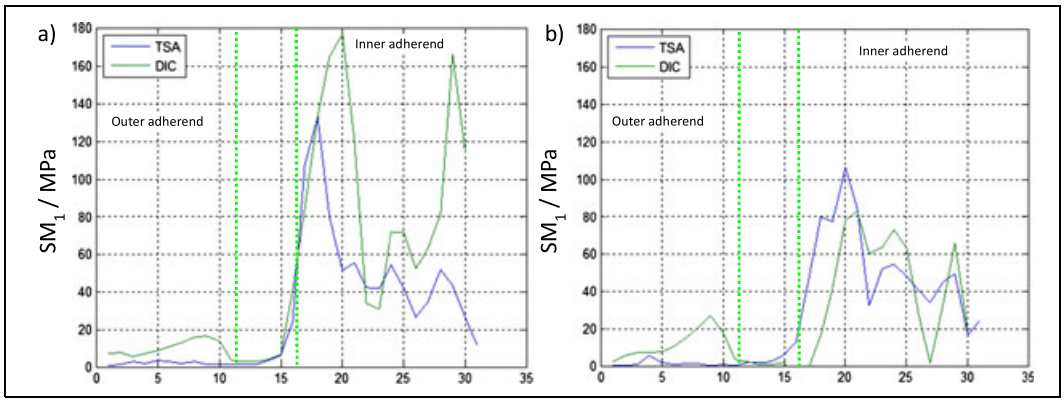

Figure 8: Stress plots through lines (a) A and (b) B shown in Figure 7

maximum values and rate of decrease in SM_1 towards the middle of the joint.

The agreement between the two data sets provides confidence in the validation of both the TSA and DIC experimental methodologies. The TSA technique is not dependent on the kinematics of the specimen, so it is not affected by out-of-plane movement. Therefore, the rather good agreement gives assurance that the strain measurements taken using the magnified 2D DIC methodology in this and other work [26, 33] are accurate and representative of the structural response. In addition to the verification of the two techniques, the agreement also provides confidence in the methodology for obtaining the elastic properties of the materials given in Table 1, as these are used in the calculation of the principal material stresses from the DIC strain data.

A separation of the two stress terms, determined from the DIC data, that form the SM_1 value given by Equation (7) is shown in Figure 9A and B. Figure 9A demonstrates the strong influence of the principal stress directions on the $K_2^p/K_1^p\sigma_2^p$ stress term (green), which is low in the outer adherend where the principal stress directions are rotated away from the x–y axes and high in the inner adherend where they are more closely aligned. Figure 9B also identifies the heavily shear-loaded interfaces between the inner and outer adherends, where the principal stress terms are the opposite of each other (i.e. close to a pure shear system), producing very little response in this region when added together to form SM_1 (red). Figure 9 illustrates a shortcoming of using TSA for model validation in systems that are close to pure shear and possible ill conditioning because of the large influence of the K_2^p/K_1^p value on SM_1 and the dominance of the σ_2^p stress term. With this in mind, the next logical step is to carry out a model validation study, examining the influence of certain parameters on the outcome; such a study is described in the Numerical Model Evaluation section.

doi: 10.1111/str.12142

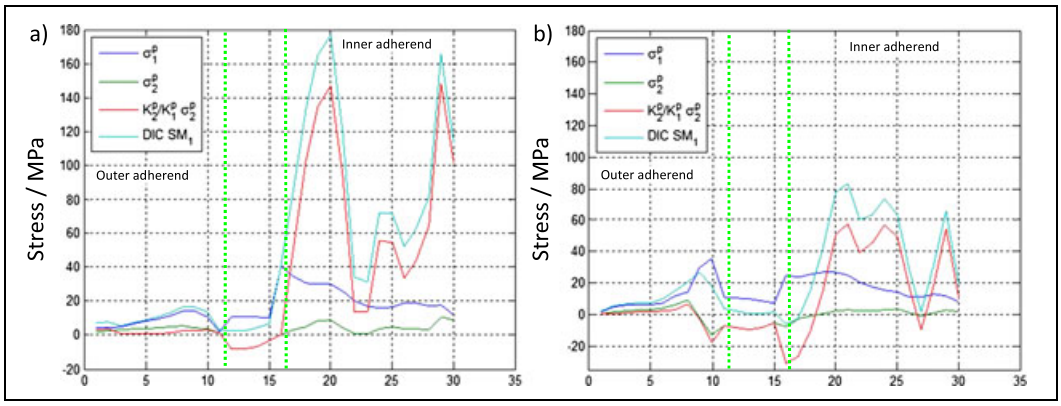

Figure 9: DIC stresses through lines (a) A and (b) B shown in Figure 7

It is now possible to examine if the x–y plane is coincident with principal material plane. K_x and K_y have been measured, and K_1^p and K_2^p have been derived using the principal stress directions from the DIC, and the principal stresses and x–y stresses have also been derived from the DIC. For comparison, plots of $K_x\Delta\sigma_x + K_y\Delta\sigma_y$ and $K_1^p\Delta\sigma_1^p + K_2^p\Delta\sigma_2^p$ are given in Figure 10A and B. If the principal material directions and the image plane axes are coincident, the images in Figure 10A and B should be identical as described by Equation (6). This is clearly not the case around the region of high shear in the outer adherend, indicating that the principal material directions and the image plane are not coincident. The difference is small and of the order of 3.2×10^{-5}, but it is measurable and gives $K_{xy} = 6.97 \times 10^{-6} \pm 3.13 \times 10^{-6}\,\text{MPa}^{-1}$. The differences in the measured quantities also clearly identify the importance of conducting the analysis of the joint using the principal stress metric SM_1, as there is no question that the shear stress is zero in the principal stress plane.

Numerical Model Evaluation

The performance of a 2D finite element approach using ANSYS 12.0 (Canonsburg, Pennsylvania, USA) is examined, determining if the 2D approach adequately captures the stress and strain distributions in the complex three-dimensional composite adhesive joint problem. A simplified 2D approach is tested to identify if computationally inexpensive and relatively simple to use numerical models are capable of accurately analysing the response of a complex composite structures such as composite joints.

A global model with the same dimensions of the joint was generated using eight-node PLANE82 elements under the plane strain condition. The geometry of the laminate layers was established from measurements of the joint using vernier callipers and micrograph inspection of the joint structure. A structured mesh containing 205 elements through the thickness of the joint was generated, and a 6-kN load applied to the end of the inner adherend. A zero displacement boundary condition was applied to the other

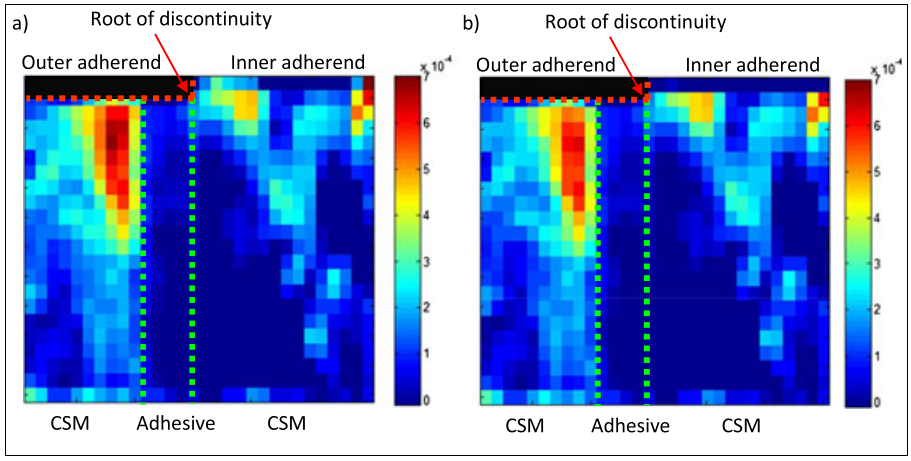

Figure 10: Product of the thermoelastic and stress terms (a) $K_1^p\Delta\sigma_1^p + K_1^p\Delta\sigma_1^p$ and (b) $K_x\Delta\sigma_x + K_y\Delta\sigma_y$

© 2015 Wiley Publishing Ltd | *Strain* (2015) **51**, 311–323
doi: 10.1111/str.12142

end of the joint, replicating the experimental loading scenario. A submodelling approach was utilised to generate a 693 934-node PLANE82 element, quarter model of the discontinuity. The submodelling method allows a highly refined mesh around the geometric discontinuity between adherends without the considerable computational expense associated with using a mesh of this density on a global model. Figure 11A shows a schematic of the submodel. The element divisions along each of the lines that form the mesh are indicated in Figure 11B. Nodal displacements through the thickness of the joint, 11.9 mm above and 13.28 mm below the discontinuity, were extracted from the global model and applied to the corresponding locations in the submodel to provide the loading and boundary conditions. A symmetrical boundary condition is applied along the vertical centreline of the joint. Full convergence studies evaluating the maximum stresses generated at the discontinuity between adherends were undertaken for both global and submodels to ensure sufficient mesh refinement. The material properties used for the model are derived from the experiments described in the Material Properties section given in Table 1.

The component stresses were output from the finite element model and manipulated into SM_1 given in Equation (7) using the same processes detailed at the beginning of the Comparison of Experimental Digital Image Correlation and Thermoelastic Stress Analysis Stress Metrics section. A plot of the finite element SM around the root of discontinuity can be seen in Figure 12.

Figure 13A and B shows very good agreement between the numerical model data and the validated experimental TSA and DIC stress metrics along lines A and B. The stress distributions through the thickness of the joint show a very similar trend to the experimental data, capturing the stress peaks in the adherends towards the adhesive layer, particularly in the outer adherend. The agreement of the line plots provides confidence in the validity of the 2D numerical modelling approach. The area of ill conditioning in the outer adherend is apparent due to the very small values of the stress metrics in this region. The only area where there is not good agreement is in the isotropic adhesive layer. Here, the thermoelastic response is a function of the sum of the principal stresses alone, which for a system in shear is zero as shown by the TSA and DIC, which is the case away from the free edge. A possible explanation offered for this is that there is a difference between the bulk and *in situ* adhesive properties; however, detailed studies using digital speckle pattern interferometry have shown that the properties of the adhesive do not change [34]. Another possible cause of the difference

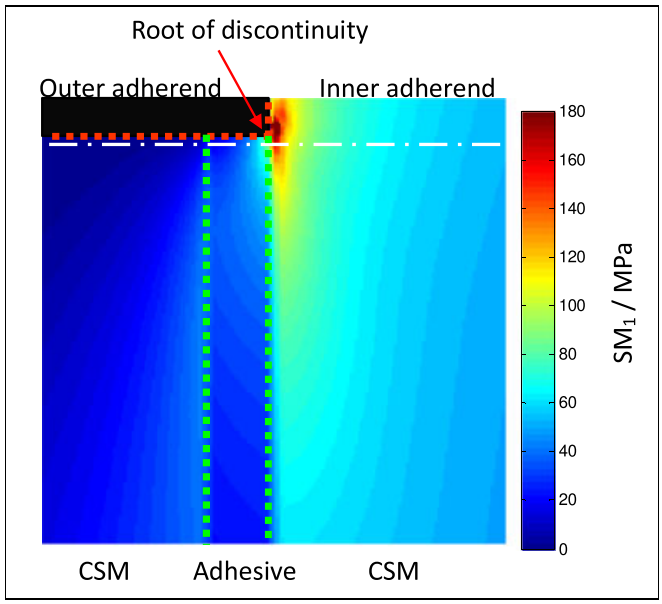

Figure 12: Finite element SM around discontinuity at 6 kN

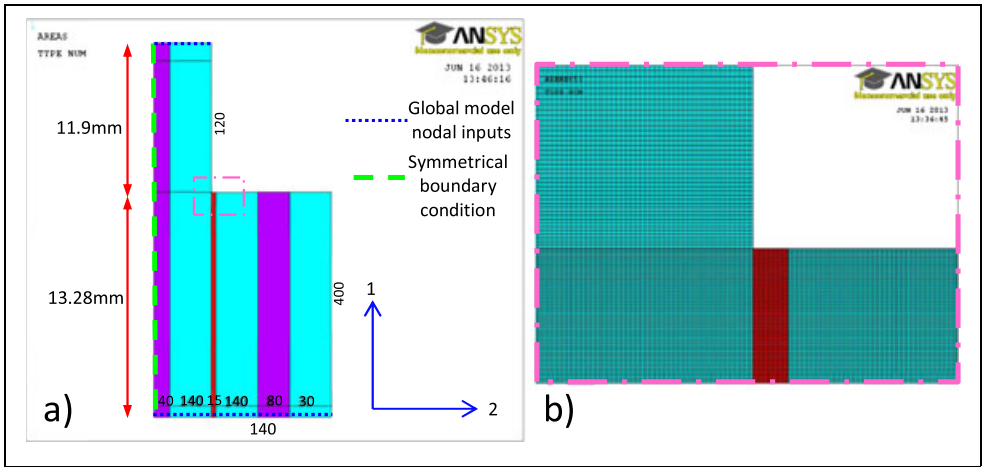

Figure 11: Schematic of the submodel and structured mesh

doi: 10.1111/str.12142

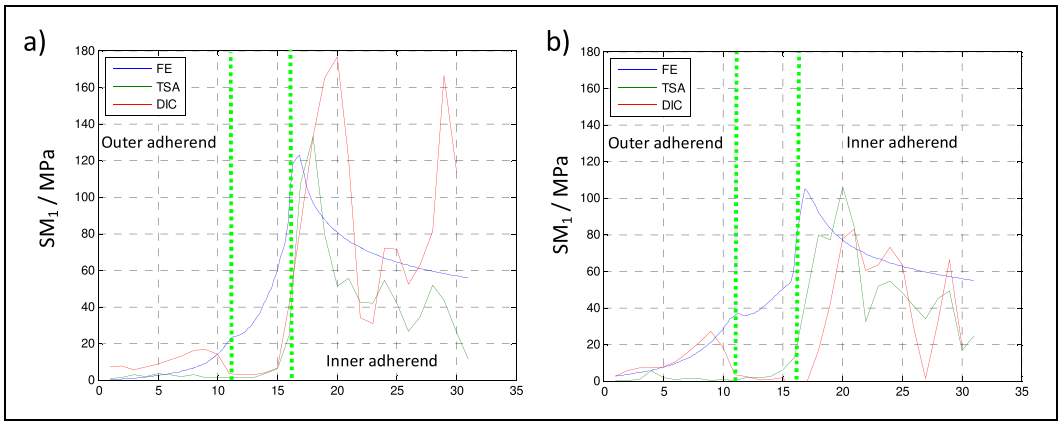

Figure 13: Comparison of SM_1 for DIC, TSA and finite element (FE) through lines (a) A and (b) B shown in Figure 7

between the experimental and numerical results in the adhesive region may be due to inaccuracies in the boundary conditions close to the numerical singularity at the discontinuity in the 2D model. A further possibility is that the fidelity of the experimental data may not be sufficient to capture the large stress gradients that occur close to the free edge resulting in zero shear and axial stresses alongside a large transverse (i.e. peel stress). This is an area that requires further investigation in the future. Overall, the model appears to quickly and accurately predict the load transfer across the joint and provide analysis of the stress concentrations in the composite around the bondline. This information may be useful to determine if delamination or fibre tear failure may occur around the bondline under load, which as a tool during initial static stressing analysis of large bonded assemblies may be sufficient.

Conclusions

Thermoelastic stress analysis and DIC were undertaken to evaluate the stress and strain distributions around the geometric discontinuity in an adhesively bonded composite DBSJ. Initial results are obtained using both techniques. To compare the results and hence perform a verification of both techniques, it was necessary to transform the DIC data into the same form as the TSA data. A new methodology was developed to calculate the TSA SM using thermoelastic constants transformed to the principal stress direction within the joint on a point-by-point basis for both the TSA and DIC data. The direction of the principal stress used in the transformation is provided by using a point-wise 'Mohr's circle analysis' of the component stresses evaluated from the DIC strain data and experimentally derived material property values. Application of the new methodology was demonstrated to be essential when evaluating complex composite structures, as small changes in the principal stress direction away from the material axes can yield large changes in the measured SM and large discrepancies in the measured values.

Comparison of the DIC and TSA stress metrics shows very good agreement, providing an important verification of the two experimental techniques. The agreement shows the 2D mesoscale DIC technique to be a powerful tool for the analysis of complex composite structures featuring small yet critical localised stress and strain concentrations.

The verified data sets are used to evaluate the performance of a computationally inexpensive 2D finite element modelling approach. Good agreement was seen between the model and the verified experimental data sets, providing confidence in this model to accurately predict the load transfer across the joint; however, further work is required to assess the differences between experimental and numerical results observed across the adhesive layer.

ACKNOWLEDGEMENTS

The work described in this paper was supported by the UK Engineering and Physical Sciences Research Council under grant number EP/G042403/1 and by a Stanley Grey Fellowship awarded by the Institute of Marine Engineering, Science and Technology.

References

1. Banea, M. D., and da Silva, L. F. M. (2009) Adhesively bonded joints in composite materials: an overview. *Proc. Inst. Mech. Eng. Part L J. Mater. Des. Appl.* **223**, 1–18.
2. Daniel, I., and Ishai, O. (2005) *Engineering Mechanics of Composite Materials*. Oxford University Press.
3. Dulieu-Barton, J. M. (2012) Chapter 8: thermoelastic stress analysis. In: *Optical Methods for Solid Mechanics* (P. Rastogi and E. Hack, Eds). Wiley, Berlin.
4. Sutton, M. A., Orteu, J.-J. and Schreier, H. W. (2009) Image correlation for shape, motion and deformation measurements: basic concepts, theory and applications.

doi: 10.1111/str.12142

5. Dulieu-Smith, J. M., Quinn, S., Shenoi, R. A., Read, P. J. C. L., and Moy, S. S. J. (1997) Thermoelastic stress analysis of a GRP tee joint. *Appl. Compos. Mater.* **4**, 283–303.
6. Boyd, S. W., Dulieu-Barton, J. M., Thomsen, O. T., and Gherardi, A. (2008) Development of a finite element model for analysis of pultruded structures using thermoelastic data. *Compos. Part A Appl. Sci. Manuf.* **39**, 1311–1321.
7. Boyd, S. W., Dulieu-Barton, J. M., Thomsen, O. T., and El-Gazzani, S. (2010) Through thickness stress distributions in pultruded GRP materials. *Compos. Struct.* **92**, 662–668.
8. Haghani, R. (2010) Analysis of adhesive joints used to bond FRP laminates to steel members – a numerical and experimental study. *Constr. Build. Mater.* **24**, 2243–2251.
9. Katnam, K. B., Dhôte, J. X., and Young, T. M. (2013) Experimental analysis of the bondline stress concentrations to characterize the influence of adhesive ductility on the composite single lap joint strength. *J. Adhes.* **89**, 486–506.
10. Backman, D., Martinez, M., Renaud, G., Genest, M. and Chisholm, K. (2007) Thermoelastic stress analysis to detect disbonding in a composite patch. in *SEM Annual Conference & Exposition on Experimental and Applied Mechanics*. Springfield, MA.
11. Becchetti, M., Flori, R., Marsili, R. and Rossi, G. L. (2009) Stress and strain measurements by image correlation and thermoelasticity, in *SEM Annual Conference & Exposition on Experimental & Applied Mechanics*.
12. Crump, D. A., and Dulieu-Barton, J. M. (2010) Performance assessment of aerospace sandwich secondary structure panels using thermoelastic stress analysis. *Plast. Rubber Compos.* **39**, 137–147.
13. Zhang, Y., Genest, M., Backman, D., Johnston, A., Komus, A., and Singh, M. (2012) Impact and compression after impact tests of a carbon/epoxy composite. In: *Failure in Composites* (A. M. Waas, B. V. Sankar and M. W. Hyer, Eds). DEStech Publications Inc. **4**. ISBN: 978-1-60595-088-4
14. Bodelot, L., Sabatier, L., Charkaluk, E., and Dufrénoy, P. (2009) Experimental setup for fully coupled kinematic and thermal measurements at the microstructure scale of an AISI 316 L steel. *Mater. Sci. Eng. A* **501**, 52–60.
15. Favier, D., Louche, H., Schlosser, P., Orgéas, L., Vacher, P., and Debove, L. (2007) Homogeneous and heterogeneous deformation mechanisms in an austenitic polycrystalline Ti–50.8 at.% Ni thin tube under tension. Investigation via temperature and strain fields measurements. *Acta Mater.* **55**, 5310–5322.
16. Maynadier, A., Poncelet, M., Lavernhe-Taillard, K., and Roux, S. (2011) One-shot measurement of thermal and kinematic fields: infrared image correlation (IRIC). *Exp. Mech.* **52**, 241–255.
17. Chrysochoos, A., Huon, V., Jourdan, F., Muracciole, J.-M., Peyroux, R., and Wattrisse, B. (2010) Use of full-field digital image correlation and infrared thermography measurements for the thermomechanical analysis of material behaviour. *Strain* **46**, 117–130.
18. Sakagami, T., Yamaguchi, N., Kubo, S., and Nishimura, T. (2008) A new full-field motion compensation technique for infrared stress measurement using digital image correlation. *J. Strain Anal. Eng. Des.* **43**, 539–549.
19. Silva, M. L., and Ravichandran, G. (2011) Combined thermoelastic stress analysis and digital image correlation with a single infrared camera. *J. Strain Anal. Eng. Des.* **46**, 783–793.
20. Silva, M. L., and Ravichandran, G. (2011) Stress field evolution under mechanically simulated hull slamming conditions. *Exp. Mech.* **52**, 107–116.
21. Reddy, J. N. (2004) *Mechanics of Laminated Composite Plates and Shells: Theory and Analysis*. 2nd edn. CRC Press, London.
22. Huntsman (2003) Private communication to Dr S. W. Boyd.
23. Huntsman (2014) Private communication to Dr S. W. Boyd.
24. Huntsman (2007) Araldite 2015 data sheet, [Online]. Available: http://www.intertronics.co.uk/data/ara2015.pdf.
25. Triconnet, K., Derrien, K., Hild, F., and Baptiste, D. (2009) Parameter choice for optimized digital image correlation. *Opt. Lasers Eng.* **47**, 728–737.
26. Crammond, G., Boyd, S. W., and Dulieu-Barton, J. M. (2014) Evaluating the localised through-thickness load transfer and damage initiation in a composite joint using digital image correlation. *Compos. Part A Appl. Sci. Manuf.* **61**, 224–234.
27. Crammond, G., Boyd, S. W., and Dulieu-Barton, J. M. (2013) Speckle pattern quality assessment for digital image correlation. *Opt. Lasers Eng.* **51**, 1368–1378.
28. Haghani, R., Al-Emrani, M. and Kliger, R. (2009) Effects of geometrical modifications on behaviour of adhesive joints used to bond CFRP laminates to steel members – experimental investigation, in *Proceedings of the Nordic Steel Construction Conference*.
29. Ruiz, P. D., Jumbo, F., Huntley, J. M., Ashcroft, I. A., and Swallowe, G. M. (2011) Experimental and numerical investigation of strain distributions within the adhesive layer in bonded joints. *Strain* **47**, 88–104.
30. Sambasivam, S. (2009) *Thermoelastic Stress Analysis of Laminated Composite Materials*. PhD thesis. University of Southampton, UK.
31. Stanley, P., and Chan, W. (1988) The application of thermoelastic stress analysis techniques to composite materials. *J. Strain Anal. Eng. Des.* **23**, 137–143.
32. Dulieu-Smith, J. M., and Stanley, P. (1994) The thermoelastic response of a thinwalled orthotropic cylinder loaded in torsion. *Proc. SEM spring Conf. Exhib.* **1**, 498–506.
33. Crammond, G., Boyd, S., and Dulieu-Barton, J. M. (2014) Dynamic analysis of composite marine structures using full-field measurement. *J. Mar. Eng. Technol.* **13**, 23–35.
34. Lilleheden, L. (1994) Mechanical properties of adhesives *in situ* and in bulk. *Int. J. Adhes. Adhes.* **14**, 31–37.

doi: 10.1111/str.12142